

MBE growth and donor doping of coherent ultrawide bandgap AlGa_N alloy layers on single-crystal AlN substrates

Cite as: Appl. Phys. Lett. **118**, 092101 (2021); doi: [10.1063/5.0037079](https://doi.org/10.1063/5.0037079)

Submitted: 10 November 2020 · Accepted: 15 February 2021 ·

Published Online: 1 March 2021





View Online



Export Citation



CrossMark

Kevin Lee,^{1,a)}  Ryan Page,²  Vladimir Protasenko,¹  Leo J. Schowalter,³  Masato Toita,³  Huili Grace Xing,^{1,2,4}  and Debdeep Jena^{1,2,4} 

AFFILIATIONS

¹School of Electrical and Computer Engineering, Cornell University, Ithaca, New York 14853, USA

²Department of Materials Science and Engineering, Cornell University, Ithaca, New York 14853, USA

³Advanced Devices Technology Center, Asahi Kasei Corporation, Hibiya Mitsui Tower, 1-1-2 Yurakucho, Chiyoda-ku, Tokyo 100-8440, Japan

⁴Kavli Institute at Cornell for Nanoscale Science, Cornell University, Ithaca, New York 14853, USA

^{a)} Author to whom correspondence should be addressed: kl833@cornell.edu

ABSTRACT

Single-crystal Aluminum Nitride (AlN) crystals enable the epitaxial growth of ultrawide bandgap Al(Ga)_N alloys with drastically lower extended defect densities. Here, we report the plasma-MBE growth conditions for high Al-composition AlGa_N alloys on single-crystal AlN substrates. An AlGa_N growth guideline map is developed, leading to pseudomorphic Al_xGa_{1-x}N epitaxial layers with $x \sim 0.6$ –1.0 Al contents at a growth rate of $\sim 0.3 \mu\text{m/h}$. These epitaxial layers exhibit atomic steps, indicating step flow epitaxial growth, and room-temperature band edge emission from ~ 4.5 to 5.9 eV . Growth conditions are identified in which the background impurity concentrations of O, C, Si, and H in the MBE layers are found to be very near or below detection limits. An interesting Si segregation and gettering behavior is observed at the epitaxial AlGa_N/AlN heterojunction with significant implications for the formation and transport of 2D electron or hole gases. Well-controlled intentional Si doping ranging from $\sim 2 \times 10^{17}$ to $3 \times 10^{19} \text{ atoms/cm}^3$ is obtained, with sharp dopant density transition profiles. In Si-doped Al_{0.6}Ga_{0.4}N epilayers, a room-temperature free electron concentration of $\sim 3 \times 10^{19} \text{ /cm}^3$, an electron mobility of $\sim 27 \text{ cm}^2/\text{Vs}$, and an n-type resistivity of $\sim 7.5 \text{ m } \Omega \text{ cm}$ are obtained. The implications of these findings on electronic and photonic devices on single-crystal AlN substrates are discussed.

Published under license by AIP Publishing. <https://doi.org/10.1063/5.0037079>

The scientific progress and technological applications of ultrawide bandgap (UWBG) semiconductors such as AlN, β -Ga₂O₃, and diamond are tied inextricably to the availability of high-quality crystalline substrates and to electronic conductivity control in epitaxial growth. Among the three UWBG semiconductor families, the AlGa_N family offers alloying heterostructure formation with doping across the largest bandgap span while maintaining the single phase.¹ The consequence of this is the burgeoning application of this material family in deep-UV photonics in LEDs, photodetectors, and lasers.^{2–5} While much of the initial development of AlGa_N semiconductors has occurred by growth on sapphire substrates, the recent availability of single-crystal AlN substrates enables rapid advances to unleash the true potential of this UWBG semiconductor family.^{6–8} This development mirrors

what is occurring with single-crystal GaN substrates of the same semiconductor family in power electronics.

Because of these advances, the epitaxial growth and conductivity control of highly crystalline Al(Ga)_N alloys on single-crystal AlN substrates have the potential to take advantage of several favorable properties ranging from the high thermal conductivity to greatly reduced defect densities.^{9–13} In addition to enabling deep-UV photonic devices, single-crystal AlN substrates, in turn, promise electronic devices such as high-voltage diodes and transistors, as well as ultrafast transistors for future applications in power electronics and microwave devices and circuits. In such devices that handle and manipulate enormous amounts of energy in small volumes and high speeds, the electrically insulating nature of AlN and the lack of thermal boundaries and high thermal conductivity of the bulk AlN substrate are very important.^{14–16}

Foundational work on the homoepitaxial growth of AlN and of AlGa_xN alloys on single-crystal AlN substrates has been performed by metal-organic chemical vapor deposition (MOCVD).^{17–19} Recently, GaN quantum dot formation on single-crystal AlN substrates was studied by NH₃-MBE.^{20,21} For growth of AlN on bulk crystals, the significant hurdle of clean homoepitaxial nucleation was overcome by the method of Al polishing, and a growth phase diagram was developed.^{22,23} In this work, the MBE growth conditions, doping, and conductivity of coherent AlGa_xN alloy layers on single-crystal AlN are presented. An AlGa_xN guideline map is developed in combination with an AlN growth phase diagram, which identifies conditions that lead to ~120-nm-thick pseudomorphic Al_xGa_{1-x}N layers with the Al composition ranging from $x \sim 0.6$ –1.0. The epitaxial AlGa_xN layers exhibit atomic steps, are coherently strained, and exhibit spectra that indicate energy bandgaps ranging from 4.5 to 5.9 eV. Furthermore, silicon doping and high n-type electrical conductivity are achieved with extremely low background impurity levels in Al_{0.63}Ga_{0.37}N epilayers. An interesting Silicon segregation effect at AlN/AlGa_xN heterojunctions is observed in the doping studies.

2" wafer single-crystal bulk Al-polar AlN substrates with dislocation density $< 10^4 \text{ cm}^{-2}$ from Crystal IS were diced into $1 \times 1 \text{ cm}^2$ pieces for MBE growth studies. The details of the *ex situ* and *in situ* cleaning processes prior to epitaxy were reported in our recent work.^{22,23} A Veeco GENXplor plasma-assisted MBE system is used here for epitaxial growth. Aluminum, gallium, and silicon are provided through standard effusion cells. Ultrahigh purity nitrogen gas is supplied at 200 W plasma power at 1.85 sccm flow, corresponding to a growth rate of $0.31 \mu\text{m/h}$. Before AlN and AlGa_xN growths, Al and Ga desorption tests are performed to ensure that consistent growth temperatures are obtained between samples and to maintain transferability of this growth mode between different MBE systems by avoiding the differences in thermocouple temperatures.²³

For all samples, a $1 \mu\text{m}$ -thick-AlN buffer layer is first grown under Al-rich conditions at 1014°C thermocouple temperature as shown in Fig. 1(a). The RF-plasma is then turned off, and the substrate temperature is raised to 100°C higher than the growth temperature to desorb the excess Al droplets. This process is monitored through reflection high energy electron diffraction (RHEED). For the growth of the AlGa_xN alloy layers right after the growth of the AlN layer, ensuring the surface is free of Al-droplets is necessary to avoid unintentional compositional grading in the subsequent AlGa_xN layers because Al can incorporate with unity probability in AlGa_xN.²⁴ After the desorption of the excess Al, the substrate temperature is reduced to the 830 – 880°C temperature window for the growth of the AlGa_xN layers. No additional Al-polishing is performed prior to AlGa_xN growth on the epitaxial AlN layer. In addition to the AlN homoepitaxial sample (A), three alloy Al_xGa_{1-x}N samples with Al of $x = 0.89$ (B), 0.86 (C), and 0.61 (D) were grown with fluxes indicated in Fig. 1(a) and layer structure shown in Fig. 1(b). The blue line in Fig. 1(a) shows the boundary between Al-rich and intermediate regimes. A similar single line does not exist for Ga desorption because we find that Ga droplets desorb faster on lower Al-content AlGa_xN surfaces, making the process dependent on the substrate chemical composition (see the supplementary material). During the AlGa_xN growth kinetics,²⁴ since Al incorporates preferentially over Ga, the growth of AlGa_xN requires the fluxes of Al and N to follow $F_{\text{Al}} < F_{\text{N}}$. The Ga-rich condition is preferred for two-dimensional growth mode.²⁵

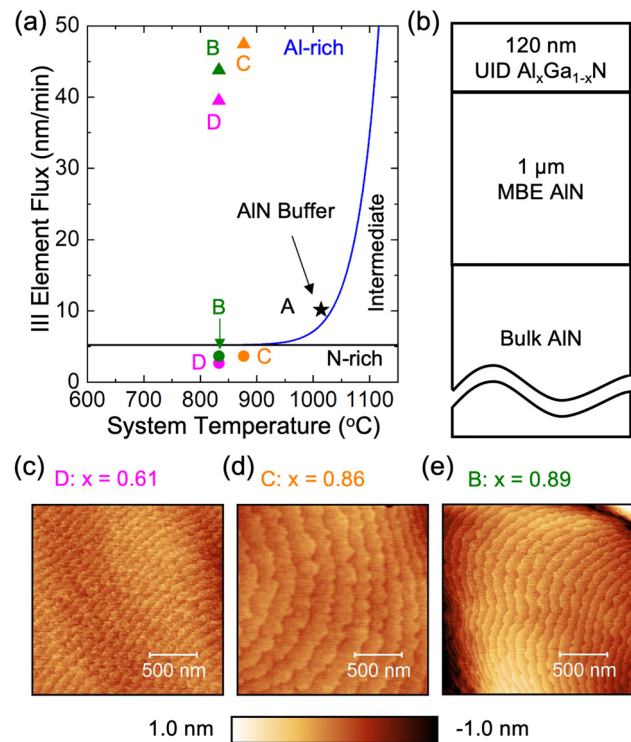


FIG. 1. (a) AlGa_xN guideline map and AlN growth phase diagram for MBE. The black star indicates the buffer Al-rich AlN growth condition. Circles are the Al flux used in the AlGa_xN layers, and triangles are the total metal flux ($F_{\text{Al}} + F_{\text{Ga}}$) during AlGa_xN growth. (b) shows the layer structure of the MBE-grown AlGa_xN and AlN on the bulk AlN substrate. (c)–(e) are $2 \times 2 \mu\text{m}^2$ AFM images of $x = 0.61$, 0.86 , and 0.89 Al content UID-Al_xGa_{1-x}N grown on bulk AlN substrates. Atomic steps are observed on all samples.

The AlGa_xN layer series with varying Al compositions grown in group III-rich conditions is shown in Fig. 1(a). The Al flux used in the growth is shown as circles and the total III element flux ($F_{\text{Al}} + F_{\text{Ga}}$) as triangles. The RHEED pattern during the AlGa_xN MBE growth remained streaky, indicating a 2D growth mode.²⁵ After the growth, Ga droplets were observed and etched away by HCl. The surface morphology measured by AFM (tapping mode, Cypher ES with FS-1500AU probe) shown in Figs. 1(c)–1(e) exhibits atomic steps with sub-nm surface roughness over $2 \times 2 \mu\text{m}^2$ scan area. The variations in the upper right and bottom left corners in Fig. 1(e) are seen more clearly in a larger area ($10 \times 10 \mu\text{m}^2$) scan presented in the supplementary material. Such features are similar to Ehrlich–Schwöbel barrier-induced step meandering, which has also been reported in homoepitaxial growth of GaN on bulk crystals by NH₃-MBE.²⁶

Figure 2(a) shows the measured high-resolution x-ray $2\theta - \omega$ spectra of the four samples performed on a Panalytical X'pert system with a triple-axis detector along the (002) direction to examine the composition and structural quality. The peak for the homoepitaxially grown AlN (sample A) is indistinguishable from the bulk substrate. The Pendellösung fringes of the alloy AlGa_xN epilayers indicate a smooth surface and a sharp interface between the AlGa_xN and AlN.²⁷ Fitting the peaks under fully strained condition yields an AlGa_xN layer

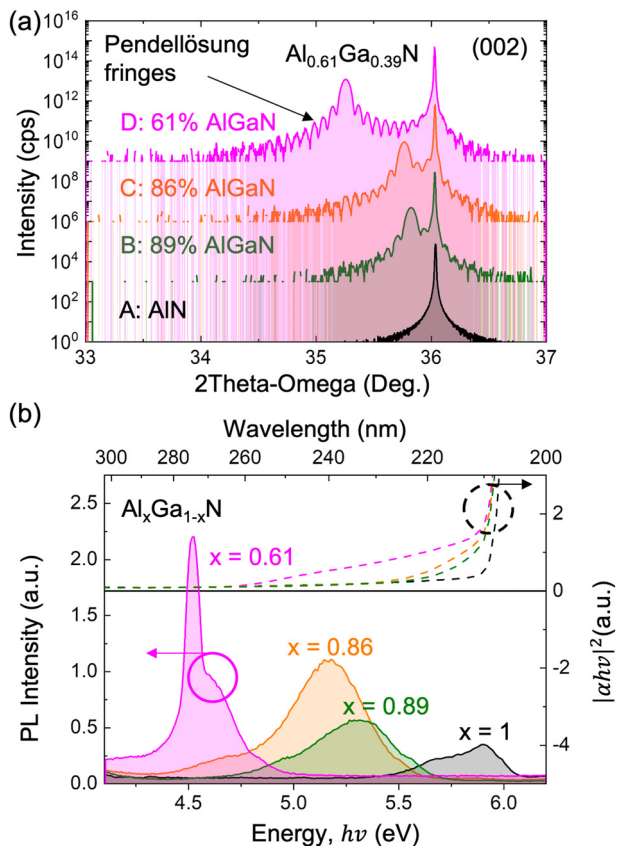


FIG. 2. (a) High resolution x-ray 2θ - ω scans along the (002) direction for $x = 0.89$ (green), 0.86 (orange), and 0.61 $\text{Al}_x\text{Ga}_{1-x}\text{N}$ (pink). The composition is determined from fitting the experimental data with simulation. (b) Solid lines are room temperature photoluminescence spectra of $\text{Al}(\text{Ga})\text{N}$ layers. Dashed lines are the UV-Vis Tauc plot. PL emission peak agrees with the absorption band edges.

thickness of ~ 120 nm with compositions of $x = 0.89$, 0.86 , and 0.61 $\text{Al}_x\text{Ga}_{1-x}\text{N}$ for samples B, C, and D, respectively. This thickness is corroborated by scanning transmission electron microscopy (STEM) images (not shown).

Room-temperature photoluminescence (PL) spectra were measured for all four samples using a pulsed ArF excimer laser excitation at 193 nm with 2 mJ energy and a repetition rate of 100 Hz on the top side of the sample. The emitted light was collected from the side of the wafer. Figure 2(b) shows the room-temperature PL and UV-Vis Tauc plot for the AlN homoepitaxial layer and the three AlGaN epitaxial layers showing the expected increase in the bandgap with the increasing Al content. The PL emission peaks range from 210 nm (5.9 eV) for AlN (sample A) to 274 nm (4.52 eV) for $\text{Al}_{0.61}\text{Ga}_{0.39}\text{N}$ (sample D). UV-Vis absorption Tauc plot spectra (dashed lines) show band edges that roughly correspond to the peaks in the PL spectra.²⁸ The emission spectrum of the $\text{Al}_{0.61}\text{Ga}_{0.39}\text{N}$ layer shows a multi-peak behavior, which could potentially be due to alloy fluctuations (see the report by Collins *et al.*,²⁹) and needs further study. The PL intensity of the AlGaN layer decreases with the increasing Al composition. Coli *et al.* observed a similar reduction in $\text{Al}_x\text{Ga}_{1-x}\text{N}$ layers with Al from $x = 0.3$

to 0.7 , which they attributed to enhanced nonradiative efficiency.³⁰ Table S.1 shows a summary of the growth conditions and properties of the epilayers in this study and similar samples grown on a GEN10 PA-MBE system, highlighting the transferability and reproducibility of the growth across systems.

To analyze the strain state of the AlGaN grown on bulk AlN , we measured the reciprocal-space maps (RSMs) of the x-ray diffraction patterns. Figures 3(a)–3(c) show the RSM spectra along the (105) peak of the AlN . The $\text{Al}_x\text{Ga}_{1-x}\text{N}$ layer peaks for $x = 0.6$ – 0.9 are aligned to AlN vertically suggesting the same Q_x value, confirming that the ~ 120 nm AlGaN layers have the same in-plane lattice constant as the AlN substrate, indicating a fully strained film. The out-of-plane reciprocal space lattice constant Q_z moves closer to the AlN peak as the Al composition increases in AlGaN from samples D to B. The RSM confirmation of fully strained condition corroborates the accuracy of the assumption in $2\theta - \omega$ scans for the extraction of the Al composition. Grandusky and Dalmau *et al.* have shown that ~ 500 nm $\text{Al}_{0.6}\text{Ga}_{0.4}\text{N}$ and 360 nm $\text{Al}_{0.81}\text{Ga}_{0.19}\text{N}$ can be grown pseudomorphically on single crystal AlN substrates by MOCVD^{31,32} in spite of the fact that for $\text{Al}_{0.6}\text{Ga}_{0.4}\text{N}$, the critical thickness is estimated to be ~ 40 nm using the Matthews–Blakeslee method. Thus, our observations by MBE confirm the prior observations by MOCVD that high Al composition AlGaN layers can remain fully strained on bulk AlN substrates well beyond the Matthews–Blakeslee limit. Rudinsky *et al.* have pointed out that the possible reason for such a large critical thickness may be due to the absence of dislocations in the substrate and different relaxation processes.³³

Next, the impurity incorporation in MBE-grown $\text{Al}_{0.63}\text{Ga}_{0.37}\text{N}$ films on bulk AlN was studied. A SIMS stack (sample E) was grown using the homoepitaxial growth conditions mentioned above. The silicon cell temperature was varied in steps separated by unintentional-doped (UID) AlGaN spacers to study the sharpness of the doping profiles, which are needed in electronic and photonic devices. Figure 4(a) shows the SIMS profiles of hydrogen, silicon, oxygen, and carbon. The detection limits are 1 – 2×10^{17} atoms/cm³ for H, 1 – 2×10^{16} atoms/cm³ for Si and C, and 6×10^{16} atoms/cm³ for O for AlGaN layers. The atomic concentration of Al and Ga is indicated on the right axis.

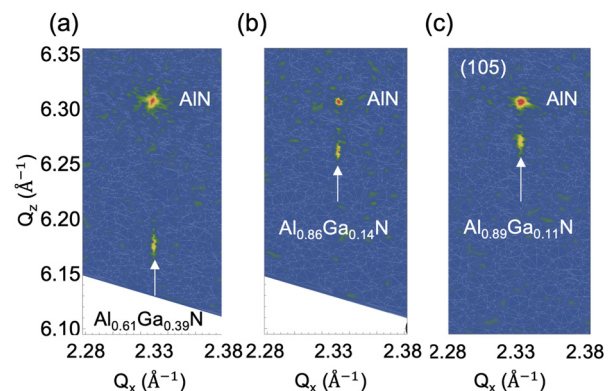


FIG. 3. X-ray reciprocal-space mapping of ~ 120 -nm-thick $\text{Al}_x\text{Ga}_{1-x}\text{N}$ (a) $x = 0.61$, (b) $x = 0.86$, and (c) $x = 0.89$ along the (105) direction on the bulk AlN substrate. Note that all Al composition AlGaN layers are fully strained to AlN .

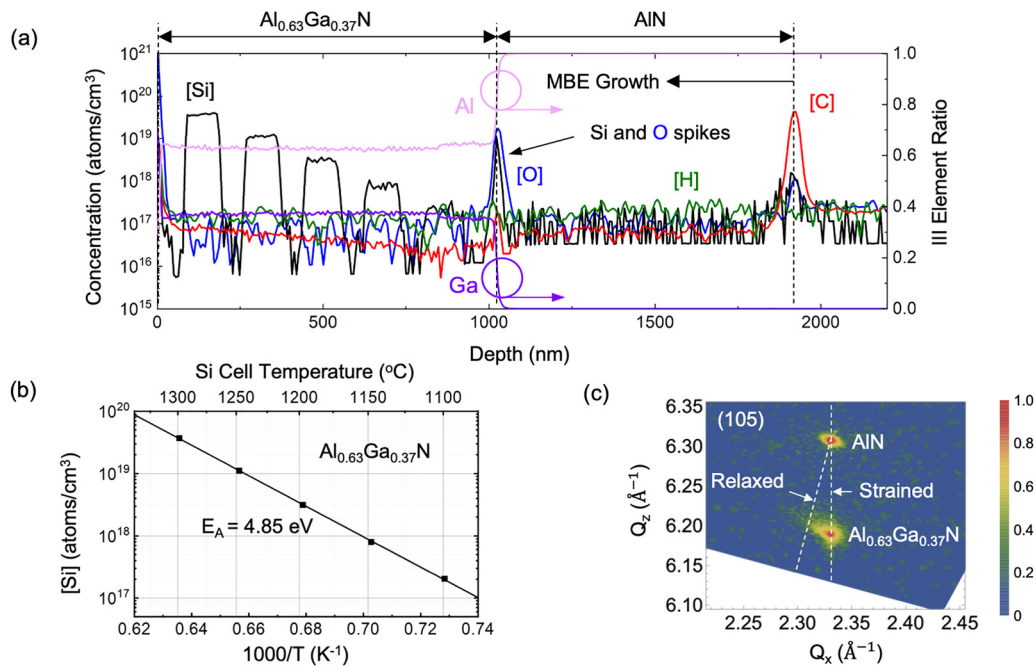


FIG. 4. (a) SIMS profile of O (blue), Si (black), H (green), and C (red) impurities in $\text{Al}_{0.63}\text{Ga}_{0.37}\text{N}$ and AlN grown on the bulk AlN substrate. The pink and purple lines are Al and Ga markers, respectively. Plateaus in AlGaN are Si-doped regions. Note that spikes of Si and O exist at the AlGaN and AlN interface. (b) Arrhenius plot of Si doping level vs Si cell temperatures. (c) X-ray reciprocal-space mapping on the Si-doped $\text{Al}_{0.63}\text{Ga}_{0.37}\text{N}$ SIMS stack. The slanted white dashed line indicates the fully relaxed AlGaN layers. Partial relaxation is observed.

The MBE-grown AlN buffer layer is 1 μm thick, and the subsequent 1- μm -thick $\text{Al}_x\text{Ga}_{1-x}\text{N}$ layer has an Al composition of $x = 0.63$.

We discuss the unintentional impurities first. A large carbon peak of $\sim 4 \times 10^{19}$ atoms/ cm^3 exists at the nucleation interface. We have reported recently that the C is likely present on the surface prior to the growth and cannot be removed by Al-assisted cleaning.²³ First principles calculations by Gorczyca *et al.* indicate a formation energy of AlN of ~ 3.9 eV,³⁴ and for Al-rich AlN growth, the formation energies of substitutional C impurities for Al and N sites are 8.6 and 1.9 eV, respectively. This suggests the possibility that C can be incorporated into the N-sites of AlN at the nucleation interface.

Density spikes of Si and O are also observed in the MBE-grown heterojunction between AlGaN and AlN. The O spike likely occurs during the growth interrupt and its origin is still under investigation. On the other hand, the Si spike is expected from thermodynamic analysis. Hoke *et al.* have argued that Si incorporation into AlN is not favorable under Al-rich growth conditions. The equation describing this reaction is $\text{Si} + 4/3 \text{AlN} \rightarrow 1/3 \text{Si}_3\text{N}_4 + 4/3 \text{Al}$, with an associated Gibbs free energy $\Delta G = +144.7$ kJ/mol, suggesting that the reaction is not spontaneous.³⁵ On the contrary, Si incorporation in GaN is possible through the mechanism $\text{Si} + 4/3 \text{GaN} \rightarrow 1/3 \text{Si}_3\text{N}_4 + 4/3 \text{Ga}$ with Gibbs free energy $\Delta G = -134.7$ kJ/mol. Therefore, the Si contamination at the nucleation interface “floats” on the growth front of the AlN under the Al-rich growth condition. As soon as an AlGaN layer is grown, Si readily incorporates into the crystal by replacing Ga sites. This behavior has also been observed for AlGaN/GaN/AlN heterostructures grown on the SiC substrate.^{36,37} The silicon spike decays to below the background level within 50 nm from this heterojunction.

The UID $\text{Al}_{0.63}\text{Ga}_{0.37}\text{N}$ layer has near detection limit levels of Si, O, and H. The apparent C impurity density is seen to increase slightly from the detection limit up to 7×10^{16} atoms/ cm^3 near the surface though it is not clear if this is introduced during growth or is a tail from the surface contamination after the MBE growth.

The Si doping concentrations inside the homoepitaxial $\text{Al}_{0.63}\text{Ga}_{0.37}\text{N}$ layer for five Si cell temperatures ranging from 1100 to 1300 $^\circ\text{C}$ are seen in Fig. 4(a). The plateaus indicate controlled doping concentrations over the range of $\sim 2 \times 10^{17}$ – 3.7×10^{19} atoms/ cm^3 . Figure 4(b) shows that the Si doping density depends on the Si cell temperature via an Arrhenius relation with an activation energy of 4.85 eV. For the highest Si doping plateau of 3.7×10^{19} atoms/ cm^3 , the Si concentration drops to 2×10^{16} atoms/ cm^3 within ~ 13 nm. A sharp Si doping profile with a slope of 3.98 nm/decade is achieved. An RSM measurement performed on the Si-doped AlGaN SIMS stack helped identify its strain state, as shown in Fig. 4(c). The peak of the $\sim 1 \mu\text{m}$ $\text{Al}_{0.63}\text{Ga}_{0.37}\text{N}$ is aligned to the AlN substrate along the Q_x direction. However, the peak diffuses to the upper right direction, suggesting that a slight relaxation occurs in the AlGaN layer.

A separate 120 nm Si-doped $\text{Al}_{0.6}\text{Ga}_{0.4}\text{N}$ layer with Si cell temperature at 1275 $^\circ\text{C}$ (sample F) was grown on a 1 μm AlN buffer on bulk AlN to evaluate electrical conductivity. The Hall-effect measurement was performed on this sample in a van der Pauw geometry. An electron mobility of ~ 27 cm^2/Vs and an electron density of $\sim 3.1 \times 10^{19}$ cm^{-3} at room temperature were measured, corresponding to a resistivity of 7.5 m Ω cm. This value is comparable to the lowest reported electrical resistivity in $\text{Al}_{0.7}\text{Ga}_{0.3}\text{N}$ grown on sapphire by Fan *et al.*³⁸

We discuss the implications of the impurity incorporation observed in the MBE-grown pseudomorphic AlGa_xN and AlN layers studied here for potential device applications. It is known that C impurity absorbs UV light at 265 nm,³⁹ leading to optical losses in UV LEDs or lasers. Growing sufficiently thick AlN buffer to separate the optical mode from the C impurity peak at the nucleation interface is, therefore, necessary. Oxygen is a shallow donor in GaN. However, there is no direct evidence that oxygen can provide conduction in high Al-content Al_xGa_{1-x}N layers. Mattila and Nieminen⁴⁰ and Van de Walle *et al.*⁴¹ both pointed out that oxygen should have DX-type behavior for Al_xGa_{1-x}N ($x > 0.2$) instead of shallow donor.

Controlling n-type doping of Si in high Al-content AlGa_xN is important for electronic devices. During metal-rich growth by MBE, Si can only be incorporated in Ga-containing GaN or AlGa_xN layers and not in binary AlN layers. Because the Si floats in metal-rich AlN, methods to prevent it from unintentional incorporation at interfaces [such as the AlN/AlGa_xN interface seen in Fig. 4(a)] must be ensured for conductivity control. It is especially important to prevent this from happening if a high-density 2D electron or hole gas is desired at the heterojunction for electronic devices such as n-channel or p-channel FETs.^{42,43} The unintentional silicon incorporation can compensate the formation of 2D hole gases or degrade the mobility of 2D electron gases. These problems can be avoided, for example, by growing a high Al-content buried AlGa_xN layer to getter the impurity far from the active heterojunctions. As shown in Fig. 4(a), the Si level can be reduced to below the detection limit within 50 nm of UID Al_{0.63}Ga_{0.37}N. To check the possibility of an electrically conducting channel formed at the unintentional Si spike, we performed Hall-effect measurements on the 120 nm UID Al_{0.61}Ga_{0.39}N (Sample D). We found it to be highly insulating. This result confirms that a high Al-content UID AlGa_xN layer can indeed serve as an effective pseudomorphic impurity gettering layer.

In summary, we have developed the MBE growth conditions for pseudomorphic Al_xGa_{1-x}N ($x \sim 0.6$ – 0.9) layers on single-crystal AlN bulk substrates that exhibit atomic steps and PL emission in the 210–278 nm window and bandgaps of 4.5–5.9 eV. The unintentional chemical impurity densities are found to be very low near the detection limits of SIMS. Doping studies indicate that Si does not incorporate in Al-rich AlN layers and only incorporates in Ga-containing AlGa_xN layers. Controlled silicon-doping densities ranging from 2×10^{17} to 3.7×10^{19} atoms/cm³ are achieved with a sharp doping slope of 3.98 nm/decade. In Si-doped Al_{0.6}Ga_{0.4}N, an electron density of 3.1×10^{19} /cm³ is achieved with a mobility of ~ 27 cm²/V s and a resistivity of 7.5 mΩ cm. The implications of unintended Si incorporation at UWBG AlN/Al(Ga)N heterojunctions on devices were discussed, and ways to prevent adverse effects were pointed out.

See the [supplementary material](#) for the Ga droplet desorption rate on different Al composition AlGa_xN surfaces, $10 \times 10 \mu\text{m}^2$ AFM image of Al_{0.89}Ga_{0.11}N, and summary table for the growth parameters and properties of AlGa_xN samples shown in this study.

The authors at Cornell University acknowledge financial support from Asahi Kasei, the Cornell Center for Materials Research (CCMR)—a NSF MRSEC program (No. DMR-1719875); ULTRA, an Energy Frontier Research Center funded by the U.S. Department of Energy (DOE), Office of Science, Basic Energy

Sciences (BES), under Award No. DE-SC0021230; and AFOSR Grant No. FA9550-20-1-0148. This work uses the CESI Shared Facilities partly sponsored by NSF No. MRI DMR-1631282 and Kavli Institute at Cornell (KIC).

DATA AVAILABILITY

The data that support the findings of this study are available from the corresponding author upon reasonable request.

REFERENCES

- ¹K. B. Nam, J. Li, M. L. Nakarmi, J. Y. Lin, and H. X. Jiang, *Appl. Phys. Lett.* **84**, 5264 (2004).
- ²N. Lobo-Ploch, F. Mehnke, L. Sulmoni, H. K. Cho, M. Guttman, J. Glaab, K. Hilbrich, T. Wernicke, S. Einfeldt, and M. Kneissl, *Appl. Phys. Lett.* **117**, 111102 (2020).
- ³H. Hirayama, T. Yatabe, N. Noguchi, T. Ohashi, and N. Kamata, *Appl. Phys. Lett.* **91**, 071901 (2007).
- ⁴D. Kim, S. Han, J. Jung, Y. Baek, J. Son, K. Lee, and J. Heo, *Opt. Express* **27**, 37446 (2019).
- ⁵T. Takano, Y. Narita, A. Horiuchi, and H. Kawanishi, *Appl. Phys. Lett.* **84**, 3567 (2004).
- ⁶P. Lu, R. Collazo, R. F. Dalmau, G. Durkaya, N. Dietz, B. Raghathamachar, M. Dudley, and Z. Sitar, *J. Cryst. Growth* **312**, 58 (2009).
- ⁷R. T. Bondokov, S. G. Mueller, K. E. Morgan, G. A. Slack, S. Schujman, M. C. Wood, J. A. Smart, and L. J. Schowalter, *J. Cryst. Growth* **310**, 4020 (2008).
- ⁸M. Bickermann, B. M. Epelbaum, O. Filip, P. Heimann, S. Nagata, and A. Winnacker, *Phys. Status Solidi C* **7**, 21 (2010).
- ⁹Z. Ren, Q. Sun, S. Y. Kwon, J. Han, K. Davitt, Y. K. Song, A. V. Nurmikko, H. K. Cho, W. Liu, J. A. Smart, and L. J. Schowalter, *Appl. Phys. Lett.* **91**, 051116 (2007).
- ¹⁰M. Martens, F. Mehnke, C. Kuhn, C. Reich, V. Kueller, A. Knauer, C. Netz, C. Hartmann, J. Wollweber, J. Rass, T. Wernicke, M. Bickermann, M. Weyers, and M. Kneissl, *IEEE Photonics Technol. Lett.* **26**, 342 (2014).
- ¹¹K. Ban, J. I. Yamamoto, K. Takeda, K. Ide, M. Iwaya, T. Takeuchi, S. Kamiyama, I. Akasaki, and H. Amano, *Appl. Phys. Express* **4**, 052101 (2011).
- ¹²I. Bryan, Z. Bryan, S. Washiyama, P. Reddy, B. Gaddy, B. Sarkar, M. H. Breckenridge, Q. Guo, M. Bobea, J. Tweedie, S. Mita, D. Irving, R. Collazo, and Z. Sitar, *Appl. Phys. Lett.* **112**, 062102 (2018).
- ¹³Z. Zhang, M. Kushimoto, T. Sakai, N. Sugiyama, L. J. Schowalter, C. Sasaoka, and H. Amano, *Appl. Phys. Express* **12**, 124003 (2019).
- ¹⁴M. Qi, G. Li, S. Ganguly, P. Zhao, X. Yan, J. Verma, B. Song, M. Zhu, K. Nomoto, H. Xing, and D. Jena, *Appl. Phys. Lett.* **110**, 063501 (2017).
- ¹⁵T. Nanjo, M. Takeuchi, M. Suita, Y. Abe, T. Oishi, Y. Tokuda, and Y. Aoyagi, *Appl. Phys. Express* **1**, 011101 (2008).
- ¹⁶S. Hashimoto, K. Akita, T. Tanabe, H. Nakahata, K. Takeda, and H. Amano, *SEI Tech. Rev.* **71**, 83 (2010), available at <https://global-sei.com/technology/tr/bn71/pdf/71-14.pdf>.
- ¹⁷A. Rice, R. Collazo, J. Tweedie, R. Dalmau, S. Mita, J. Xie, and Z. Sitar, *J. Appl. Phys.* **108**, 043510 (2010).
- ¹⁸I. Bryan, Z. Bryan, S. Mita, A. Rice, L. Hussey, C. Shelton, J. Tweedie, J. P. Maria, R. Collazo, and Z. Sitar, *J. Cryst. Growth* **451**, 65 (2016).
- ¹⁹T. Sakai, M. Kushimoto, Z. Zhang, N. Sugiyama, L. J. Schowalter, Y. Honda, C. Sasaoka, and H. Amano, *Appl. Phys. Lett.* **116**, 122101 (2020).
- ²⁰P. Sohi, D. Martin, and N. Grandjean, *Semicond. Sci. Technol.* **32**, 075010 (2017).
- ²¹S. Tamariz, G. Callsen, and N. Grandjean, *Appl. Phys. Lett.* **114**, 082101 (2019).
- ²²Y. Cho, C. S. Chang, K. Lee, M. Gong, K. Nomoto, M. Toita, L. J. Schowalter, D. A. Muller, D. Jena, and H. G. Xing, *Appl. Phys. Lett.* **116**, 172106 (2020).
- ²³K. Lee, Y. Cho, L. J. Schowalter, M. Toita, H. G. Xing, and D. Jena, *Appl. Phys. Lett.* **116**, 262102 (2020).
- ²⁴E. Iliopoulos and T. D. Moustakas, *Appl. Phys. Lett.* **81**, 295 (2002).
- ²⁵V. N. Jmerik, E. V. Lutsenko, and S. V. Ivanov, *Phys. Status Solidi A* **210**, 439 (2013).

- ²⁶N. A. K. Kaufmann, L. Lahourcade, B. Hourahine, D. Martin, and N. Grandjean, *J. Cryst. Growth* **433**, 36 (2016).
- ²⁷A. L. Holmes, K. G. Fertitta, F. J. Ciuba, and R. D. Dupuis, *Electron. Lett.* **30**, 1252 (1994).
- ²⁸B. D. Vezibicke, S. Patel, B. E. Davis, and D. P. Birnie, *Phys. Status Solidi B* **252**, 1700 (2015).
- ²⁹C. J. Collins, A. V. Sampath, G. A. Garrett, W. L. Sarney, H. Shen, M. Wraback, A. Y. Nikiforov, G. S. Cargill, and V. Dierolf, *Appl. Phys. Lett.* **86**, 031916 (2005).
- ³⁰G. Coli, K. K. Bajaj, J. Li, J. Y. Lin, and H. X. Jiang, *Appl. Phys. Lett.* **78**, 1829 (2001).
- ³¹J. R. Grandusky, J. A. Smart, M. C. Mendrick, L. J. Schowalter, K. X. Chen, and E. F. Schubert, *J. Cryst. Growth* **311**, 2864 (2009).
- ³²R. Dalmau, B. Moody, R. Schlessler, S. Mita, J. Xie, M. Feneberg, B. Neuschl, K. Thonke, R. Collazo, A. Rice, J. Tweedie, and Z. Sitar, *J. Electrochem. Soc.* **158**, H530 (2011).
- ³³M. E. Rudinsky, A. V. Lobanova, S. Y. Karpov, and R. A. Talalaev, *Jpn. J. Appl. Phys., Part 1* **58**, SC1017 (2019).
- ³⁴I. Gorczyca, A. Svane, and N. E. Christensen, *Phys. Rev. B* **60**, 8147 (1999).
- ³⁵W. E. Hoke, A. Torabi, J. J. Mosca, and T. D. Kennedy, *J. Vac. Sci. Technol. B* **25**, 978 (2007).
- ³⁶W. E. Hoke, A. Torabi, J. J. Mosca, R. B. Hallock, and T. D. Kennedy, *J. Appl. Phys.* **98**, 084510 (2005).
- ³⁷C. Poblentz, P. Waltereit, S. Rajan, U. K. Mishra, J. S. Speck, P. Chin, I. Smorchkova, and B. Heying, *J. Vac. Sci. Technol. B* **23**, 1562 (2005).
- ³⁸Z. Y. Fan, J. Y. Lin, and H. X. Jiang, in *Quantum Sensing and Nanophotonic Devices IV*, edited by M. Razeghi and G. J. Brown (SPIE, 2007), p. 64791I.
- ³⁹R. Collazo, J. Xie, B. E. Gaddy, Z. Bryan, R. Kirste, M. Hoffmann, R. Dalmau, B. Moody, Y. Kumagai, T. Nagashima, Y. Kubota, T. Kinoshita, A. Koukitu, D. L. Irving, and Z. Sitar, *Appl. Phys. Lett.* **100**, 191914 (2012).
- ⁴⁰T. Mattila and R. M. Nieminen, *Phys. Rev. B* **54**, 16676 (1996).
- ⁴¹C. G. Van de Walle, C. Stampfl, J. Neugebauer, M. D. McCluskey, and N. M. Johnson, *MRS Internet J. Nitride Semicond. Res.* **4**, 890 (1999).
- ⁴²A. Hickman, R. Chaudhuri, S. J. Bader, K. Nomoto, K. Lee, H. G. Xing, and D. Jena, *IEEE Electron Device Lett.* **40**, 1293 (2019).
- ⁴³R. Chaudhuri, S. J. Bader, Z. Chen, D. A. Muller, H. G. Xing, and D. Jena, *Science* **365**, 1454 (2019).

MBE growth and donor doping of coherent ultrawide bandgap AlGaN alloy layers on single-crystal AlN substrates

Supplementary Information

Kevin Lee

Fig. S1(a) shows the layer structure of the $\text{Al}_{0.89}\text{Ga}_{0.11}\text{N}$ sample labeled (B) in the main text. We observed a step meandering effect on all the high Al-content AlGaN layers grown on single-crystal AlN substrates, as shown in Fig. S1(b). A root-mean-square surface roughness of 1 nm is measured for the scanned area shown.

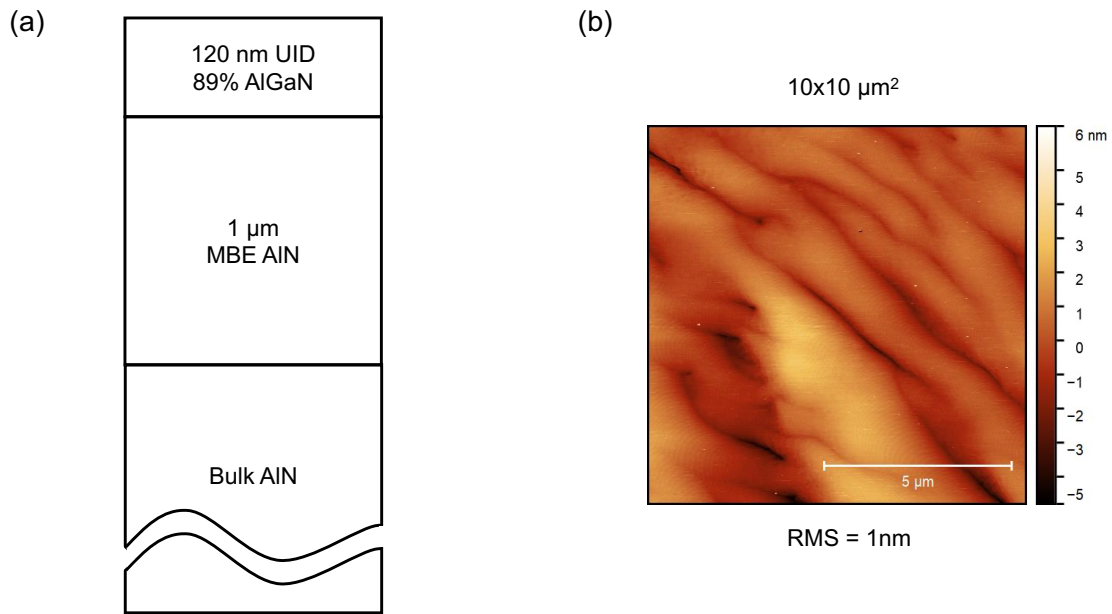


Figure S1. (a) Epitaxial layer structure of $\text{Al}_{0.89}\text{Ga}_{0.11}\text{N}$ grown on single-crystal AlN substrate. (b) shows a $10 \times 10 \mu\text{m}^2$ AFM image of the grown sample.

The Ga droplet desorption rate on an AlGa_xN layer surface is determined using a method similar to that described in our previous work for Al desorption process on AlN.¹ We grew a series of Al_xGa_{1-x}N layers with $x = 1, 0.8, 0.6, 0.4, 0.2,$ and 0 and measured the Ga droplet desorption rate (ϕ_{Ga}) on each of these surfaces individually. Fig. S2(a) shows the ϕ_{Ga} vs. substrate temperature on different Al composition AlGa_xN layers. The Arrhenius plot of Fig. S2(a) is shown in Fig. S2(b). The linear dependence observed for ϕ_{Ga} on all Al-content AlGa_xN surfaces indicates a thermally activated desorption process. The Ga droplet desorbs faster on lower Al-content AlGa_xN surface, suggesting that Ga droplets prefer to stick on higher Al-content AlGa_xN layer. Brown et al. have used quadrupole mass spectrometry to study the Ga adsorption on the Al-polar AlN surface.² They found the first monolayer of Ga adsorbate on the AlN surface has stronger bonding than on GaN surface. We emphasize that in this work we are discussing Ga droplets instead of the dynamic bilayer Ga on the surface. Hence it requires a theoretical DFT study to provide further insight behind the reason of the observed microscopic behavior.

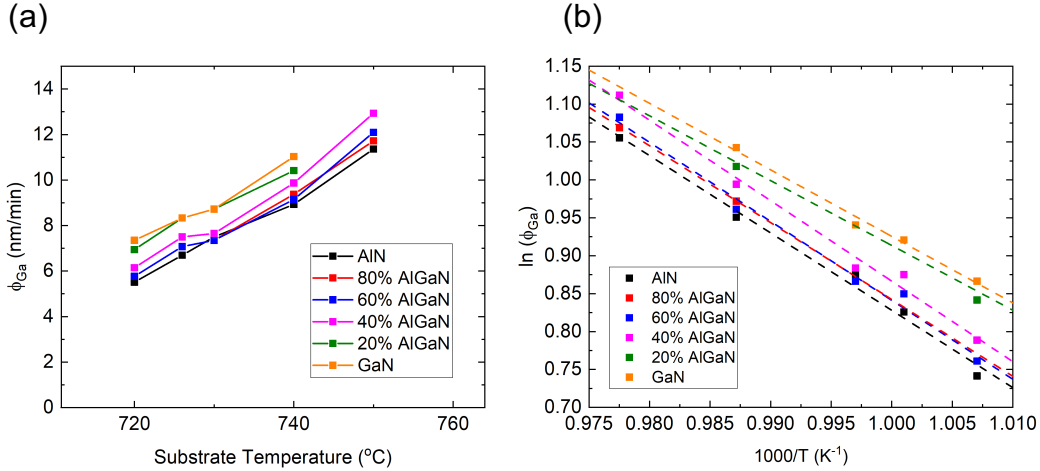


Figure S2. (a) Ga droplet desorption rate (ϕ_{Ga}) vs. substrate temperature for various Al-content AlGa_xN surfaces. (b) Arrhenius plot of the Ga droplet desorption rates.

The table below shows the growth parameters, Al compositions, PL peak wavelengths, and surface roughness of samples A – F discussed in the main text. Note that samples A – F are grown in a GENXplor PA-MBE system. Additional samples 10-A to 10-E are grown on a GEN10 PA-MBE system using a similar growth technique.

Table S.1 Summary of PL peaks and growth parameters for different Al-content AlGa_xN layers (Sample A~E). Sample 10-A~E shows a set of samples grown on a GEN10 PAMBE system, demonstrating the reproducibility of our growth techniques.

Sample	T _{Sub} (°C)	Al content (x)	PL Peak (nm, eV)	Surface Roughness (nm)	Si Cell (°C)
A	1014	1	210 (5.9)	0.18	NA
B	877	0.89	233 (5.32)	0.3	NA
C	833	0.86	240 (5.17)	0.11	NA
D	833	0.61	274 (4.52)	0.14	NA
E	833	0.63	NA	0.12	1100 - 1300
F	833	0.6	274 (4.52)	0.4	1275
10-A	767	0.53	280 (4.43)	0.41	NA
10-B	767	0.7	263 (4.71)	0.19	1250
10-C	767	0.7	263 (4.71)	0.22	1300
10-D	767	0.79	248 (5)	1.41	1275
10-E	767	0.79	251 (4.94)	0.67	1325

Reference:

¹ K. Lee, Y. Cho, L.J. Schowalter, M. Toita, H.G. Xing, and D. Jena, *Appl. Phys. Lett.* **116**, 262102 (2020).

² J.S. Brown, G. Koblmüller, R. Averbek, H. Riechert, and J.S. Speck, *J. Vac. Sci. Technol. A Vacuum, Surfaces, Film.* **24**, 1979 (2006).